# Hysteresis phenomena in the interaction process of conical shock waves: experimental and numerical investigations

By G. BEN-DOR[1], E. I. VASILIEV[2], T. ELPERIN[1]
AND A. CHPOUN[3]

[1]Pearlstone Center for Aeronautical Engineering Studies, Department of Mechanical Engineering,
Ben-Gurion University of the Negev, Beer Sheva, Israel

[2]Department of Computational Mechanics, Volgograd University, Volgograd, Russia

[3]Laboratoire d'Aérothermique du CNRS, Meudon, France

The interaction of two conical shock waves, one converging and straight and the other diverging and curvilinear, in an axisymmetric flow was investigated both experimentally and numerically. A double-loop hysteresis was discovered in the course of the experimental investigation. The double-loop hysteresis consisted of a major one, associated with the interaction between the boundary layer and the wave configuration, and a minor one, associated with the dual-solution phenomenon, which is known to be non-viscous-dependent. The minor hysteresis loop was found to be an internal hysteresis loop of the major one. As expected the numerical Euler calculations failed to detect the viscous-dependent major hysteresis loop but did succeed in obtaining the non-viscous-dependent minor (internal) hysteresis loop. In addition, multiple hysteresis loops, associated with the interaction between the shock wave configuration and the edge of the curvilinear mobile cone were also observed. The non-viscous minor hysteresis loop involved different overall shock wave reflection configurations, and the other hysteresis loops involved the same shock wave reflection configuration but different flow patterns.

## 1. Introduction

Mach (1878) discovered experimentally that the reflection of oblique shock waves in steady flows could result in two types of wave configurations, namely regular reflection (RR) and Mach reflection (MR). Von Neumann (1945) suggested two extreme criteria for the transition between these two types of wave configurations. They were later named the *detachment criterion* and the *von Neumann criterion*. These two criteria bound a domain inside which both the RR and the MR wave configurations are theoretically possible. For this reason this domain was termed the *dual-solution domain*. Hornung, Oertel & Sandeman (1979) were the first to hypothesize that the existence of a dual-solution domain could lead to a hysteresis in the RR ↔ MR transition. Chpoun *et al.* (1995) recorded experimentally for the first time a hysteresis in the reflection of symmetric shock waves. Chpoun & Lengrand (1997) and Li, Chpoun & Ben-Dor (1999) recently recorded a similar hysteresis in the reflection of asymmetric shock waves.

In spite of the good to excellent agreement which was evident when the above-

mentioned experimentally recorded hysteresis processes were compared with pre-dictions based on two-dimensional analytical models (see e.g. Chpoun *et al.* 1995 and Li *et al.* 1999) it was claimed by Skews, Vukovic & Draxl (1996), Fomin *et al.* (1996), Skews (1997, 1998) and Ivanov *et al.* (1998*a, b*) that the above-mentioned experimentally recorded hysteresis processes in the RR $\leftrightarrow$ MR transition were trig-gered by three-dimensional edge effects, and hence could not be considered as purely two-dimensional.

For this reason it was decided to design an experimental set-up by which the question of whether a hysteresis in the RR $\leftrightarrow$ MR transition could exist in a flow field which, by definition, is free of three-dimensional effects. The experimental set-up fulfilling this requirement is shown schematically in figure 1(*a*). An incident converging straight conical shock wave, $i_1$, was generated using a conical ring with a sharp leading edge having an angle, $\theta$. This converging straight conical shock wave interacted with a diverging curvilinear conical shock wave, $i_2$, which was generated by a curvilinear cone. Owing to the fact that the angle of interaction between these two conical shock waves depends on the axial distance between the conical ring and the curvilinear cone, the interaction between these two conical shock waves led to the formation of either a regular (RR) or a Mach reflection (MR). By continuously moving the curvilinear cone along the axis of symmetry, the angle of interaction between the two conical shock waves was changed and as a result both the RR $\rightarrow$ MR and the MR $\rightarrow$ RR transitions were observed and recorded.

Incidentally, Krasil'nikov (1991) investigated experimentally the interaction between a converging and a diverging quasi-uniform conical shock wave in axisymmetric supersonic flows using a similar experimental set-up (see figure 1*b*). Unlike our set-up, in his a straight rather than a curvilinear cone was used in order to generate the diverging conical shock wave, $i_2$. As a result, in his experiments, an incident converging straight conical shock wave interacted with a diverging straight conical shock wave. The interaction of these two conical shock waves also led to the formation of either a regular (RR) or a Mach reflection (MR). However, his experimental study was not aimed at investigating the MR $\leftrightarrow$ RR transition process.

The experimental and numerical flow fields, obtained when a curvilinear cone is immersed in a supersonic flow, are shown in figures 2(*a*) and 2(*b*), respectively. (Details regarding both the experimental and the numerical investigations are given in the following.) The strength of the diverging curvilinear conical shock wave engulfing the curvilinear cone varies along its front. The diverging curvilinear conical shock wave, which is very weak near the nose of the curvilinear cone, reaches a maximum strength just above the edge of the curvilinear cone, at which an expansion fan is formed. The expansion fan interacts with the diverging curvilinear conical shock wave and reverses its curvature. Since the strength of the diverging curvilinear conical shock wave changes along its front, different angles of interaction with the incident converging straight conical shock wave are encountered as the curvilinear cone is moved back and forth along the axis of symmetry. As will be shown subsequently, this change in the angles of interaction leads to transitions between the regular and the Mach reflection wave configurations obtained. In addition, it will be shown, both experimentally and numerically, that unlike in the case of planar shock waves where only one hysteresis loop has been found to exist, in the present case of conical shock waves there are a few hysteresis loops in the transition process. Preliminary results of the experimental study can be found in Chpoun *et al.* (1999). Our full experimental and numerical results will be presented in the following sections.

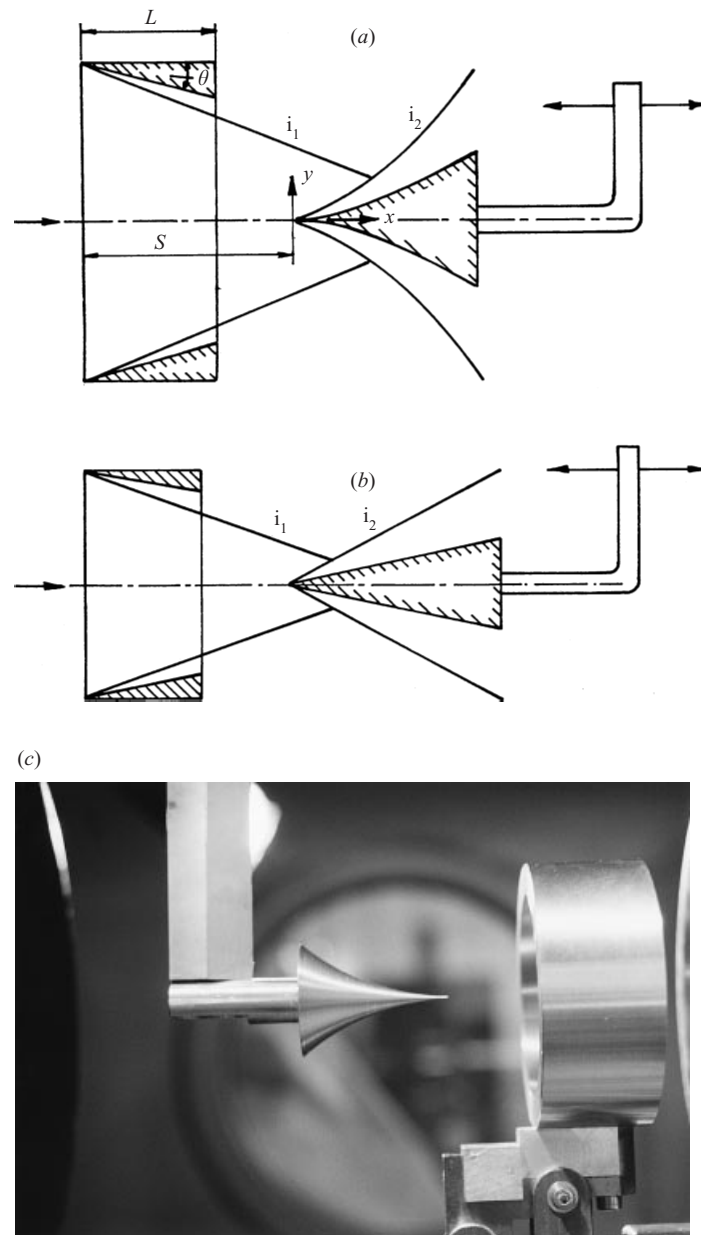It should be stressed here that unlike the above-mentioned cases of reflection of

FIGURE 1. (*a*) Schematic illustration of the experimental set-up used. An incident conical straight converging shock wave is generated using a conical ring with a sharp leading edge. This shock wave then interacts with a diverging conical curvilinear shock wave, which is generated by a curvilinear mobile cone. (*b*) Schematic illustration of a similar experimental set-up used by Krasil'nikov (1991) who experimentally investigated the interaction between converging and diverging quasi-uniform conical shock waves in axisymmetric supersonic flows. An incident conical straight converging shock wave is generated using a conical ring with a sharp leading edge. This shock wave then interacts with a diverging conical straight shock wave, which is generated by a straight mobile cone. (*c*) Photograph of the present experimental set-up.
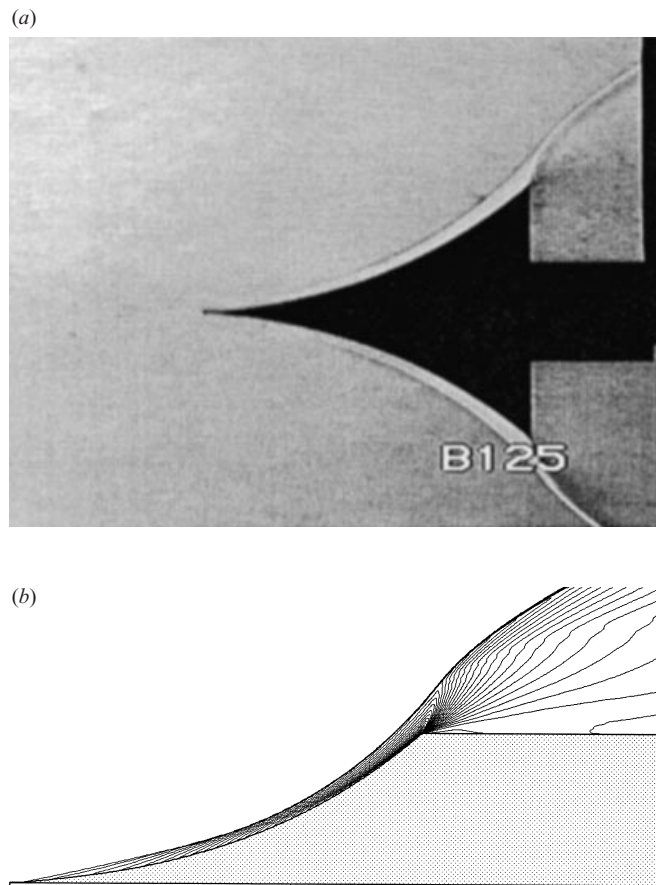
(*a*)



(*b*)



FIGURE 2. (*a*) The experimental and (*b*) the numerical flow fields, which are obtained when a curvilinear cone is immersed in a supersonic flow. Note that the strength of the diverging curvilinear shock wave engulfing the curvilinear cone varies along its front. The diverging curvilinear conical shock wave, which is very weak near the nose of the cone, reaches a maximum strength just above the rear edge of the curvilinear cone, at which a conical expansion fan is formed. The conical expansion fan interacts with the diverging curvilinear conical shock wave and reverses its curvature.

symmetric and asymmetric planar shock waves in two-dimensional plane flows where the hysteresis was recorded on the plane of symmetry, the hysteresis in the present axisymmetric flow does not occur on the axis of symmetry, at which an RR is theoretically impossible (see e.g. Rylov 1990).

## 2. The experimental study

### 2.1. *The experimental facility*

The experiments were conducted in the SH2 hypersonic wind tunnel of Laboratoire d'Aérothermique du CNRS at Meudon, France. The SH2 wind tunnel is an open jet facility that produces a uniform airflow in a continuous manner. The wind tunnel run time is virtually infinite. The nozzle exit diameter is 127 mm. The ratio of the areas of the exit and the throat sections is 25. Consequently, the test-section-flow Mach number, based on an inviscid theory, was designed to be exactly 5. However, due to viscous effects the actual flow Mach number, which was calculated from the

measurements of the stagnation pressure of the supersonic jet and the stagnation pressure behind the normal part of the bow shock formed ahead of a Pitot gauge, was $M_0 = 4.96$. This value was maintained within a variation of less than 1% along a distance of about 200 mm.

Two-stage volumetric compressors (MPR-RC300 type) supply air at the jet stagnation pressure of 8.5 bars. The flow is heated to a stagnation temperature of 453 K to avoid liquefaction during the expansion in the nozzle. A group of three parallel pumps (MPR-1000 type) evacuate the air after passing the test section. The jet static pressure is 13 mmHg and the test chamber pressure varied, depending on the model size, in the range 4–10 mmHg. This in turn resulted in a slightly under-expanded to a nearly adapted jet.

The resulting supersonic jet velocity was 870 m s$^{-1}$ and its temperature and pressure were 76.5 K and 1683 Pa, respectively. The mass flow rate was about 0.76 kg s$^{-1}$. The Reynolds number per unit length, based on these conditions, was $1.28 \times 10^7 \, \text{m}^{-1}$. This high Reynolds number minimized viscous effects and as a consequence the experimental results could be considered suitable for comparison with inviscid theories. For example, the boundary layer thickness at the end of a 100 mm long flat plate at zero angle of incidence was about 0.5 mm.

For flow visualization a colour schlieren photography system was employed. The colour pictures were obtained using a CCD camera, which was connected simultaneously to a video recorder and to a PC monitored digital picture acquisition system. For each run a video movie and a sequence of digital pictures were obtained.

The recent experimental investigations of the hysteresis in the RR ↔ MR transition by Chpoun *et al.* (1995), Chpoun & Lengrand (1997), Li *et al.* (1999) and Chpoun *et al.* (1999) were conducted on the same facility.

### 2.2. *The experimental set-up*

The specific experimental set-up for the present investigation is shown schematically in figure 1(*a*). A photograph showing both the conical ring and the curvilinear cone is shown in figure 1(*c*). The 70 mm in diameter and 28 mm wide conical ring was placed in the centre of the 127 mm supersonic jet, emanating from the wind tunnel. The head angle of the conical ring was $\theta = 8.5°$. The shape of the curvilinear cone was $y(x) = 0.000115x^3 + 0.002717x^2 + 0.08749x$ ($x$ and $y$ are in mm). This shape led to a slope of 5° at the nose of the curvilinear cone and a slope of 35° at its rear edge. These values were chosen in order to promote both the regular (RR) and the Mach reflection (MR) wave configurations. (Note that this geometry led to a cone with a very fine nose of which about 0.5–1 mm was inevitably chopped off during its manufacturing process.) The base diameter and the length (height) of the curvilinear cone were 30.4 mm and 40 mm, respectively. Both the conical ring and the curvilinear cone were manufactured from brass using CNC machine tools.

The curvilinear cone was mounted on a rod, which was perfectly aligned with the axis of symmetry. The rod was connected to a three-axis motorized traverse device. The curvilinear cone could be moved, by means of this motor, back and forth along the axis of symmetry with a velocity equal to 0.22 mm s$^{-1}$. (For this reason the curvilinear cone will be referred to in the following as the mobile cone.) A digital transducer recorded the position of the mobile cone.

As mentioned earlier, the displacement of the mobile cone resulted in a change in the angle of interaction between the incident converging straight conical, $i_1$, and the incident diverging curvilinear conical, $i_2$, shock waves. This in turn resulted in different shock wave reflection wave configurations. For convenience, a non-

dimensional distance, $X = S/L$, will be used in the following presentation. As shown in figure 1(*a*), $S$ is the distance between the entrance cross-section of the conical ring and the nose of the mobile cone, and $L$ (= 28 mm) is the width of the conical ring. Using this definition, the coordinates of the entrance and the exit cross-sections of the conical ring are $X = 0$ and $X = 1$, respectively.

### 2.3. *The experimental results*

A sequence of 10 frames taken from one of the experimentally recorded videotapes is shown in figure 3. The sequence shows the evolution of the wave pattern during the shift of the mobile cone in the course of changing $X : 1.56 \rightarrow 0.70 \rightarrow 1.68$. Three different wave patterns are seen in figure 3. At this stage, they will be termed, for simplicity, as Types A, B and C (see figure 6 and subsequent discussion).

From the initial position (frame *a*) with coordinate $X = 1.56$ the mobile cone was shifted slowly with the velocity of $0.22\,\mathrm{mm\,s^{-1}}$ along the axis of symmetry towards the conical ring. Whenever a drastic change was seen to occur, the mobile cone was stopped and the flow was allowed to stabilize. Type A wave patterns are seen near the mobile cone in frames (*a*) to (*d*). The Type A wave pattern consists of a straight incident diverging conical shock wave attached to the nose of the mobile cone. This interacts with the converging straight conical shock wave, which is generated by the conical ring. A schematic illustration of a Type A wave pattern, shown in figure 3(*a*) to (*d*), is shown in figure 4(*a*). As a result of the boundary layer separation, a large slow re-circulation zone is induced near the surface of the mobile cone. The slow re-circulation zone is the mechanism supporting the straight incident diverging conical shock wave attached to the nose of the mobile cone. In figure 4(*a*), $i_1$ and $i_2$ are the converging and the diverging incident conical shock waves, respectively, $r_1$ and $r_2$ are the reflected fronts of $i_1$ and $i_2$ after their interaction, d is the shock wave formed by the flow over the rear edge of the mobile cone (point A), s.f. denotes the separated flow zone with the slow re-circulation, and t.d. is a tangential discontinuities. The interaction of this tangential discontinuity with the reflected shock wave, $r_2$, results in a rarefaction wave, which is seen to interact with the reflected shock wave, $r_1$. The existence of the separated flow zone indicates that viscous effects play an important role in the formation of the Type A wave pattern. (As will be shown subsequently, the Euler code, which was applied in the course of the present study, failed, as expected, to reproduce the viscous-dependent Type A wave configuration. However, Burstchell *et al.* (2001), who recently simulated the present case using a Navier–Stokes code, did succeed in obtaining the above described Type A wave configuration.)

When the mobile cone is shifted from $X = 0.86$ (figure 3*d*) to $X = 0.70$ (figure 3*e*) the wave configuration changes suddenly from Type A to Type B. This transition involved the reattachment of the boundary layer and the disappearance of the separated zone. As a result the incident shock wave, attached to the nose of the mobile cone, is suddenly changed from a strong straight incident diverging conical shock wave to a weak incident diverging curvilinear conical shock wave, which was discussed earlier when figure 2 was introduced. In addition, a Mach stem, m, is formed between the converging straight conical shock wave, $i_1$, and the newly formed weak diverging curvilinear conical shock wave, $i_2$. The Type B wave configuration shown in frame (*e*), consists essentially of two triple points, which share the same Mach stem (see figure 4*b* and subsequent discussion). This transition, which will be referred to as Type A → Type B transition, occurred at $X \approx 0.78$.

The subsequent figures 3(*f–j*) correspond to the shift of the mobile cone in the reverse direction. Two transitions in the flow pattern were encountered, in the course of
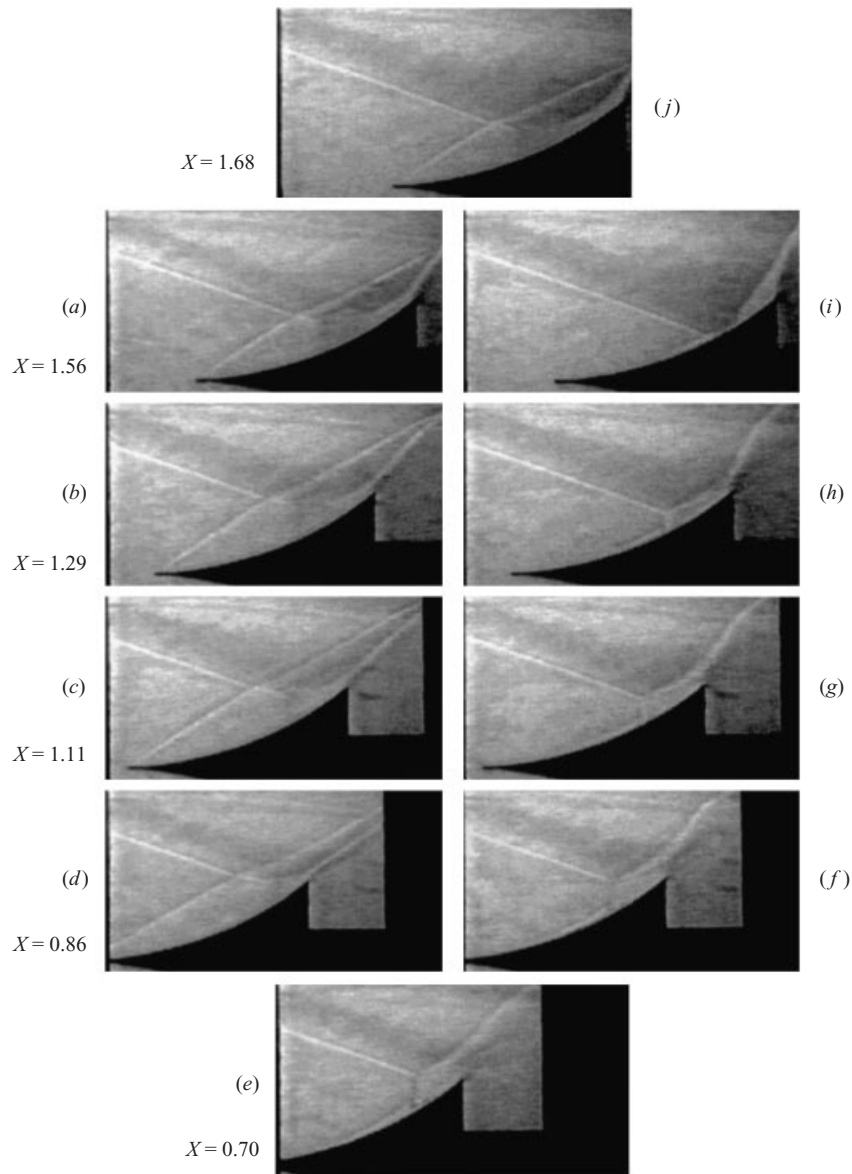
FIGURE 3. Experimental photographs illustrating the existence of a hysteresis loop in the interaction of two conical shock waves. The hysteresis consists of three different types of wave configuration: a Type A wave configuration is seen in ($a$), ($b$), ($c$), ($d$) and ($j$); a Type B wave configuration is seen in ($e$), ($f$), ($g$) and ($h$); a Type C wave configuration is seen in frame ($i$).

shifting the mobile cone from $X = 0.70$ (frame $e$) to $X = 1.68$ (frame $j$). On shifting it from $X = 0.70$ (frame $e$) to $X = 1.29$ (frame $h$) the Mach stem continuously decreased until it disappeared between $X = 1.29$ (frame $h$) and $X = 1.56$ (frame $i$), and the Type B wave pattern changed to another wave pattern, Type C. This transition, which will be referred to in the following as Type B $\rightarrow$ Type C transition, occurred at $X \approx 1.38$. The Type C wave pattern consists of an incident converging straight conical shock wave, $i_1$, which interacts with the incident weak diverging curvilinear conical shock
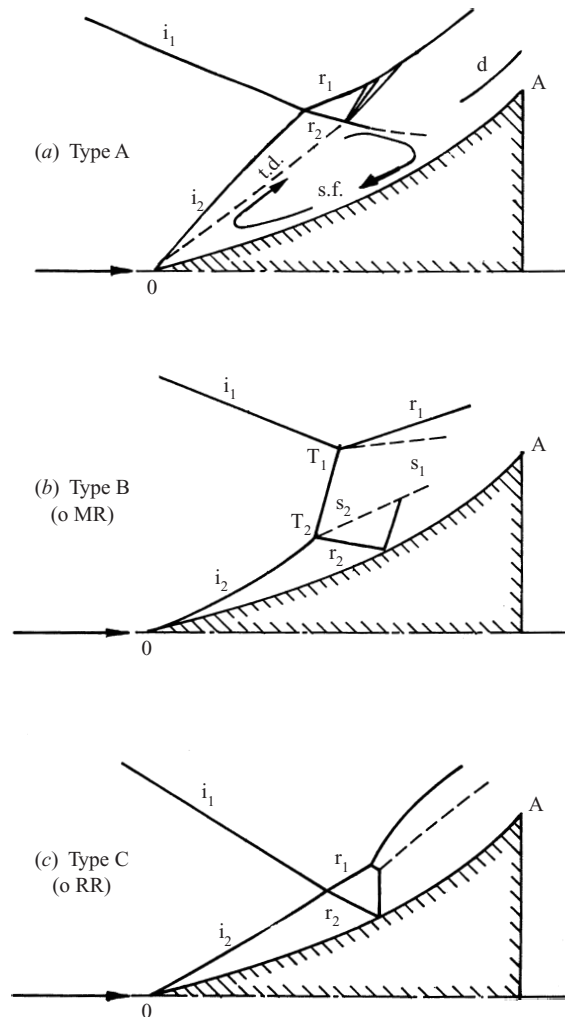
FIGURE 4. Schematic illustration of the various wave configurations which were obtained in the course of the experimental study. (*a*) A Type A wave configuration. A slow re-circulation zone exists near the surface of the mobile cone, which ensures the existence of the strong diverging conical shock wave attached to the nose of the mobile cone. The converging and the strong diverging incident conical shock waves, are $i_1$ and $i_2$, respectively; $r_1$ and $r_2$, the refracted fronts of $i_1$ and $i_2$ after their interaction, are in fact the reflected shock waves, d is the shock wave formed by the flow over the shoulder (point A) of the mobile cone, s.f. denotes a separated flow region with slow re-circulation, t.d is a tangential discontinuity. The interaction of this tangential discontinuity with the reflected shock wave, $r_2$, results in a rarefaction wave, which is seen to interact with the reflected shock wave, $r_1$; (*b*) a Type B wave configuration. The two Mach reflection wave configurations have a common Mach stem. (*c*) A Type C wave configuration. The wave configuration consists of an incident converging conical shock wave, $i_1$, generated by the conical ring, an incident weak diverging conical shock wave, $i_2$, generated by the mobile cone, and two refracted shock waves, $r_1$ and $r_2$. Note that the refracted shock wave emanating from the interaction point towards the surface of the mobile cone reflects from the surface of the mobile cone as a regular reflection.

wave, $i_2$. The interaction results in two refracted shock waves, $r_1$ and $r_2$ (see figure 4*c* and subsequent discussion). The $r_2$ shock wave is seen to reflect from the surface of the mobile cone as a regular reflection, RR. On shifting the mobile cone from $X = 1.56$ (frame *i*) to $X = 1.68$ (frame *j*) the boundary layer was separated from

the surface of the mobile cone. As a result, the incident shock wave, attached to the nose of the mobile cone, suddenly changed from a weak diverging curvilinear conical shock wave to a strong diverging straight conical shock wave, and a flow pattern with a separated flow zone, similar to that shown in frame (*a*) was formed again. This transition, which will be referred to in the following as Type C → Type A transition, occurred at $X \approx 1.61$.

Note that the pairs of frames $(a, i)$, $(b, h)$, $(c, g)$ and $(d, f)$, which correspond to the same $X$-position of the mobile cone, clearly demonstrate the existence of two different wave patterns for the same flow conditions. The entire set of frames in figure 3 provides clear experimental evidence for the existence of a hysteresis process, which consists of the following three transitions: Type A → Type B at $X \approx 0.78$ on decreasing $X$, Type B → Type C at $X \approx 1.38$ on increasing $X$, and Type C → Type A at $X \approx 1.61$ on increasing $X$. The hysteresis loop can be summarized as:

$$\text{Type A} \xrightarrow{X \approx 0.78} \text{Type B} \xrightarrow{X \approx 1.38} \text{Type C} \xrightarrow{X \approx 1.61} \text{Type A}.$$

As found in the course of the present experimental investigation the Type B → Type C transition at $X \approx 1.38$ (between frames $h$ and $i$ in figure 3) on increasing $X$, was the origin of an additional internal hysteresis loop. In order to detect this loop in some series of the experiments, immediately after encountering the Type B → Type C transition, at $X \approx 1.38$, the mobile cone was stopped and its shifting direction was reversed.

A sequence of eight experimental frames corresponding to this case is shown in figure 5. The coordinate of the mobile cone was changed in the $X$-direction: $1.39 \rightarrow 1.12 \rightarrow 1.39$. Two transitions of the wave pattern are evident. A Type C → Type B transition takes place at $X \approx 1.16$, when $X$ is changed from 1.20 (frame $c$) to 1.12 (frame $d$) and an opposite Type B → Type C transition takes place at $X \approx 1.38$, when $X$ is changed from 1.37 (frame $g$) to 1.39 (frame $h$). It should be noted here that, based on the experiments, the Type B → Type C transition (between frames $g$ and $h$) occurred when the Mach stem had a finite height. As will be shown subsequently, this was not the case in the inviscid numerical simulations, where the Mach stem decreased continuously until it vanished at the Type B → Type C transition. Probably, viscous effects behind the Mach stem are the cause for this peculiar behaviour. It is noted again that the Type C ↔ Type B hysteresis loop, shown in figure 5, is an internal hysteresis loop of the major hysteresis loop shown in figure 3. This internal hysteresis loop can be summarized as:

$$\text{Type C} \xrightarrow{X \approx 1.16} \text{Type B} \xrightarrow{X \approx 1.38} \text{Type C}.$$

Finally, it should be noted here that figure 3(*b, h*) and figure 5(*b, f*), which correspond to the same $X$-position of the mobile cone, clearly demonstrate that three different shock wave patterns, Type A, Type B and Type C, were obtained experimentally, for the same flow conditions.

These three different wave patterns, namely, Type A, Type B and Type C, are shown schematically in figures 4(*a*), 4(*b*) and 4(*c*), respectively. The Type B wave configuration, shown in figure 4(*b*), is similar to the overall Mach reflection wave configuration in the interaction of plane shock waves (see Li *et al.* 1999). It consists of two triple points and hence two Mach-reflection wave configurations. The two Mach-reflection wave configurations have a common Mach stem. For this reason the Type B wave configuration will be referred to, in the following, as an overall Mach reflection wave configuration, oMR. In the Type C wave configuration, figure 4(*c*), the
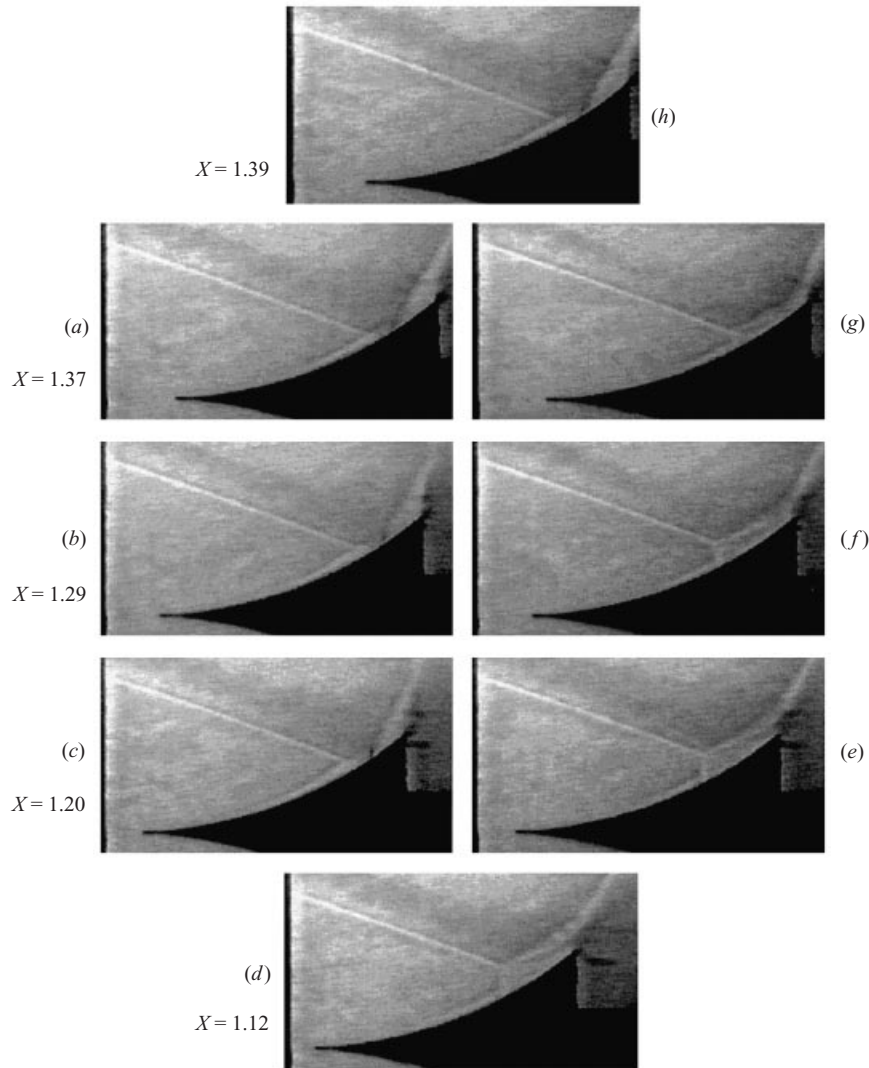
FIGURE 5. Experimental photographs illustrating the existence of an internal hysteresis loop in the interaction of two conical shock waves. The hysteresis consists of two different types of wave configuration: a Type C wave configuration is seen in (*a*), (*b*), (*c*) and (*h*); a Type B wave configuration is seen in (*e*), (*f*) and (*g*).

converging straight conical shock wave, $i_1$, is seen to interact with the weak diverging curvilinear conical shock wave, $i_2$, and to result in two refracted shock waves, $r_1$ and $r_2$. The Type C wave configuration is similar to the overall regular reflection wave configuration in the interaction of plane shock waves (see Li *et al.* 1999). For this reason the Type C wave configuration will be referred to, in the following, as an overall regular reflection wave configuration, oRR. As can be seen in figure 4(*c*), the $r_2$ shock wave reflects from the surface of the mobile cone as a regular reflection, RR.

The double-loop hysteresis described above is shown in figure 6. The frames shown in figure 3 show a viscous-dependent major hysteresis loop, which is accompanied by three transitions:
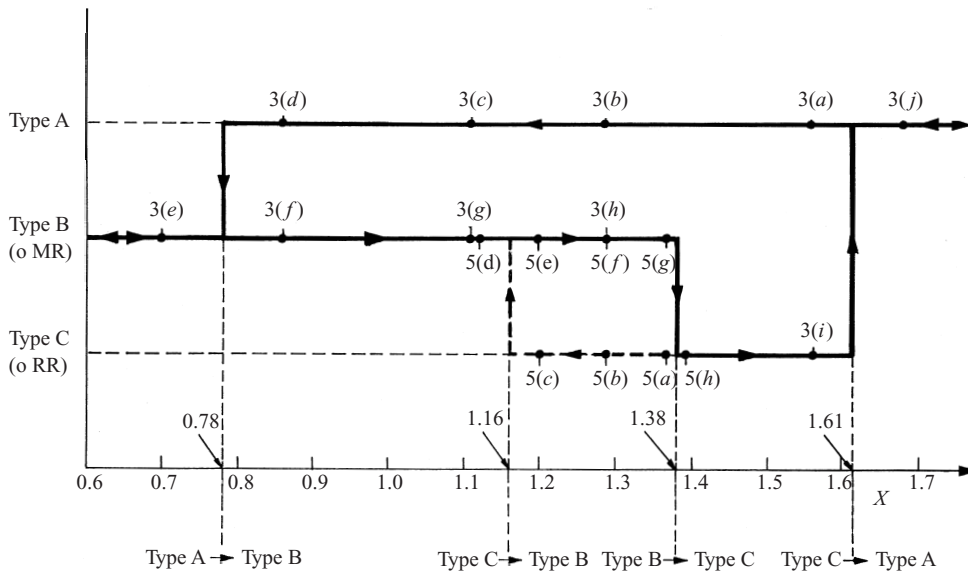
FIGURE 6. The experimentally obtained double-loop hysteresis. The experimentally recorded frames, which are shown in figures 3 and 5, are marked along the loops.

Type A → Type B transition at $X \approx 0.78$;

Type B → Type C transition at $X \approx 1.38$; and

Type C → Type A transition at $X \approx 1.61$.

Similarly, the frames shown in figure 5 describe an internal (non-viscous-dependent) hysteresis loop with two transitions.

Type B → Type C (or oMR → oRR) transition at $X \approx 1.38$ ; and a reversed

Type C → Type B (or oRR → oMR) transition at $X \approx 1.16$.

The frames shown in figures 3 and 5 are marked on figure 6, labelled according to the figure number.

Not only do the experimental results provide, for the first time, a clear proof of the existence of a hysteresis phenomenon in the oRR ↔ oMR transition in a flow field (not planar) which by definition is free of three-dimensional effects, they also reveal a complex double-loop hysteresis. As will be shown subsequently, the non-viscous-dependent internal hysteresis loop was simulated in the course of our detailed inviscid numerical investigation. In addition, multiple hysteresis loops, associated with the interaction between the shock wave configuration and the rear edge of the mobile cone were also observed.

## 3. The numerical study

### 3.1. *The numerical method*

The problem was solved using an Eulerian code for an ideal gas with $\gamma = 1.4$. The stationary solutions were determined numerically using a W-modification of the Godunov method with a second-order accuracy both in space and time. A detailed description of the W-modification of the Godunov method can be found in Vasiliev (1996). General details of the code can be also found in Ben-Dor, Elperin & Vasiliev (1999).

Godunov's method (as well as all the other methods which employ the solution
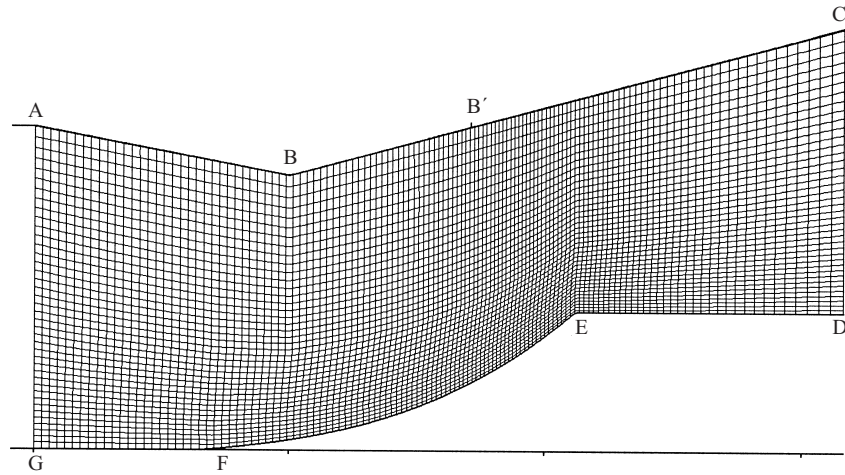
FIGURE 7. Illustration of the computational domain and the numerical grid for one of the calculations.

of the Riemann problem) is very well suited for tracking shock wave fronts. Consequently, a procedure for tracking the Mach stem was applied in the course of the present numerical calculations. This procedure transformed the mesh during the calculations in such a manner that one of the vertical boundary lines of the mesh coincided with the Mach stem. It can be seen, in figure 7, where the mesh that was used in one of the calculations is shown, that the vertical boundary lines of the mesh became curvilinear as a result of tracking the Mach stem. The numerical details of the procedure for tracking a shock wave front, i.e. transformation of the numerical mesh in such a manner that one of the vertical boundary lines of the mesh would coincide with the Mach stem, are described in Vasiliev (1999).

The tracking of the Mach stem resulted in a situation in which the mesh became movable. The most important reason for using a movable mesh was that the curvilinear cone moved during the calculations. The location of the mobile cone was changed in the range $0 \leqslant X \leqslant 2.2$ with increments of $\Delta X = 0.02$. The time interval for changing $X$ was composed of two parts: a transitional-time interval, $0.6L/a_0$, and a time interval required for reaching a stationary solution, $4L/a_0$, where $a_0$ is the speed of sound of the free stream. These time intervals were based on preliminary calculations. The criterion for determining whether a stationary solution had been reached was the stabilization of the location of the Mach stem. It was assumed that the flow attained a stationary state when the velocity at the centre of the Mach stem, $D_{\text{stem}}$, fulfilled the condition $|D_{\text{stem}}| \leqslant 0.001a_0$ during a time interval allocated for reaching a stationary solution. If at the end of the allocated time interval this condition was not met, the calculations continued.

As mentioned earlier, the numerical calculations were performed using a curvilinear moving grid, similar to that shown in figure 7. In order to increase the accuracy of the calculations the mesh was refined in the region where the interaction took place. The area occupied by the grids, i.e. ABCDEFGA, was, in fact, the control volume. For convenience, straight lines emerging from the edge of the conical ring (BC) and the back edge of the mobile cone (CD) bound the computational domain. This could be done since the flow beyond these two straight lines was supersonic and hence perturbations from these artificial boundaries could not enter the control volume.
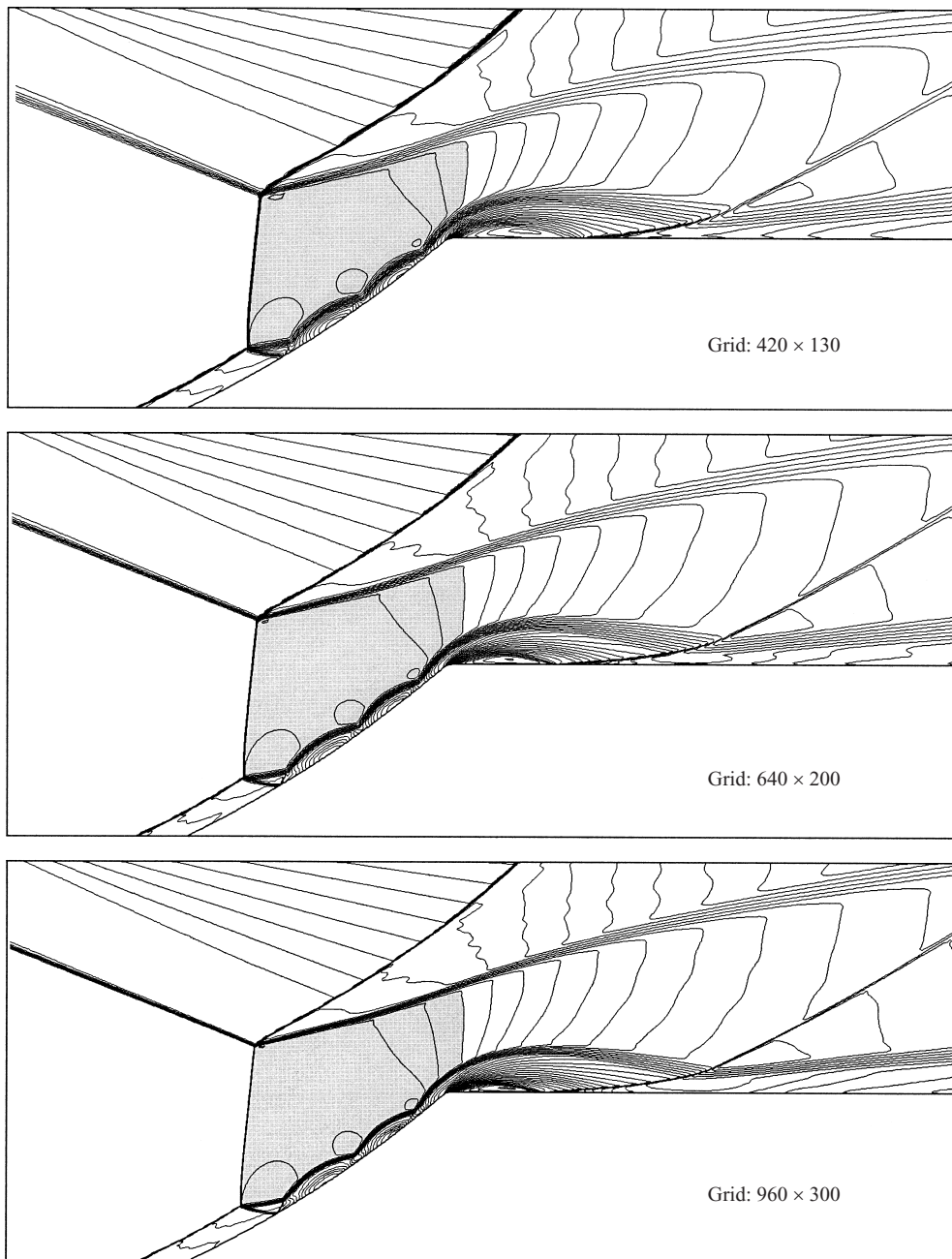
FIGURE 8. Constant flow Mach number contours as obtained using different grids. The shaded regions are subsonic. The calculations justify the use of 'soft' boundary conditions in the calculations. In addition, the results justify the use of a $640 \times 200$ mesh in most of the calculations.

This is verified in figure 8 where flow-Mach-number contour lines, in the vicinity of the edge of the mobile cone, as obtained using different grids are shown. The subsonic parts of the flow fields are shaded. The flow is supersonic in the parts of the flow fields that are not shaded (including the exit boundary). This justifies the subsequently

mentioned use of 'soft' boundary conditions in our calculations (i.e. all the derivatives with respect to the x-coordinate were set to be zero).

It is also evident from figure 8 that refining the calculation grid affected the resolution of the discontinuities (the shock waves, the contact boundary of the wall jet and the contact surface emanating from the upper triple point). The mesh refinement, in the region with the smooth flow, hardly changed the results. Note that the locations of the various shock waves and the other quantitative characteristics of the flow pattern almost coincide for the three different meshes shown in figure 8. Most of the calculations, in the course of the present study, were performed using a mesh of $640 \times 200$ (in some cases, however, a mesh of $760 \times 240$ was used).

The motion of the mobile cone was also taken into account by the boundary conditions at its surface. The normal component of the gas velocity was set to be equal to the normal component of the surface velocity of the mobile cone. Solid boundary conditions, i.e. $v_n = 0$ were used along the surface of the conical ring (AB in figure 7) and $v_n = w_n$ along the surface of the mobile cone (DEF), where $w_n$ is the normal component of the velocity of the surface of the mobile cone. Thus in the calculations, as in the experiments, the position of the mobile cone was varied smoothly with additional time delays to allow the flow to settle.

In summary the imposed boundary conditions were as follows (see figure 7):

uniform flow with $M_0 = 4.96$ along the left-hand boundary (GA), i.e. the inlet;

solid boundary conditions along the surfaces of the conical ring (AB) and the mobile cone (DEF);

'soft' boundary conditions along the right-hand boundary (CD), i.e. the outlet;

solid wall boundary conditions along the boundary BB′ and 'soft' boundary conditions along the boundary B′C, where B′ divides the boundary BC at about $1/3$ and $2/3$. It should be noted that, based on figure 8, 'soft' boundary conditions could have been imposed along the entire upper boundary (BC) but then it would have taken a longer time to reach a stationary solution. The only difference between the 'soft' and the solid wall boundary conditions is the velocity. In the 'soft' boundary conditions the derivatives of the velocity are set to be equal to zero.

### 3.2. *The numerical results*

As mentioned earlier the present numerical investigation, which was based on an inviscid code, failed, as expected, to record the viscous-dependent major hysteresis loop, shown in figure 3. However, the present numerical investigation did succeed in simulating the non-viscous-dependent internal hysteresis loop, shown in figure 5. In addition, a multi-loop hysteresis of the flow patterns was also found in the course of the numerical investigation.

The numerical simulation was done in the following way. The mobile cone was first put at $X = 0$ and the numerical code was run until a stable situation was reached. At this stage the mobile cone was slightly shifted, a distance of $\Delta X = 0.02$ from the conical ring (i.e. $X$ was increased), and the code was run until a new stable solution was again attained. This procedure was repeated until the location $X = 2.2$ was reached. At this point the direction of shifting the mobile cone was reversed (i.e. $X$ was decreased) until the initial situation, $X = 0$, was again reached. (Note that since $\Delta X = 0.02$, shifting the mobile cone from $X = 0$ to $X = 2.2$ and then back to $X = 0$ meant that a stationary solution was fully calculated at 220 positions.)

The above procedure resulted in the overall multi-loop hysteresis, which is shown in figure 9 in the $(X, H_m)$-plane. Here $H_m = h_m/L$ is the non-dimensional length of the Mach stem, where $h_m$ is the length of the Mach stem, i.e. the distance between
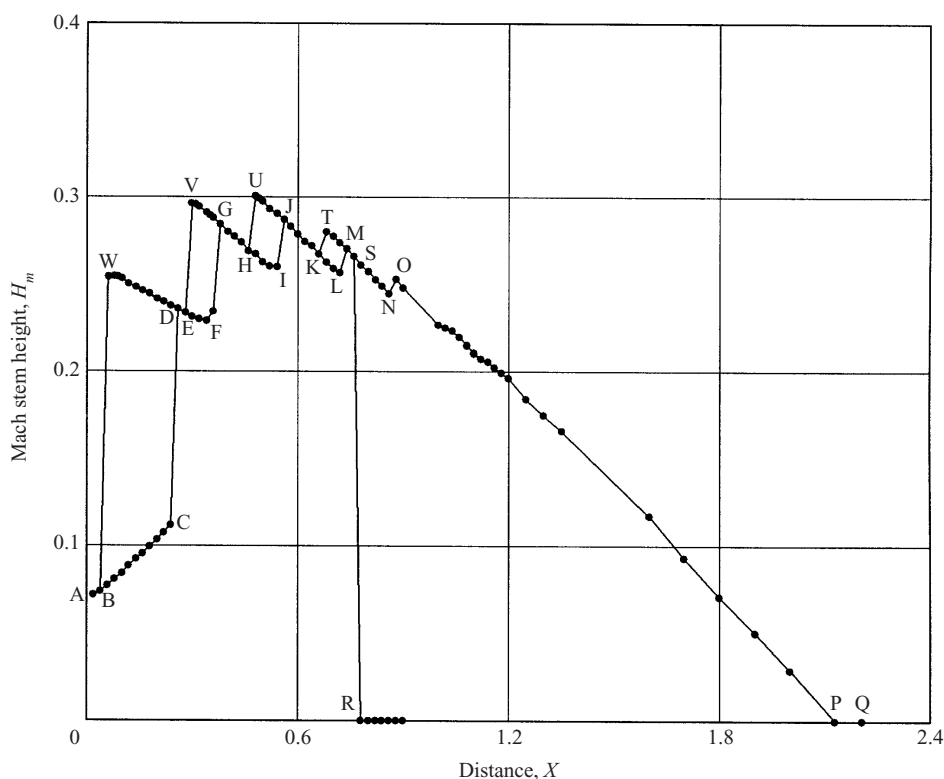
FIGURE 9. The numerically obtained multi-loop-hysteresis. The loop consists of two types of hysteresis: one major one S-N-O-P-R-S and four minor ones B-C-D-W-B, E-F-G-V-E, H-I-J-U-H and K-L-M-T-K.

the two triple points when the resulted overall wave configuration is oMR (similar to the one shown in figure 4*b*). Evidently, for an oRR wave configuration (see figure 4*c*) $H_m = 0$.

The stable flow states (see figure 9), which were encountered when the mobile cone was shifted along the $X = 0 \rightarrow 2.2$ path and the reversed $X = 2.2 \rightarrow 0$ path were A-B-C-D-E-F-G-H-I-J-K-L-M-N-O-P-Q and Q-P-R-S-M-T-K-J-U-H-G-V-E-D-W-B-A, respectively. These two different paths of stable flow states consist, as will be shown subsequently, of two different types of hysteresis loops. The first one, the major one, which is similar to the one obtained experimentally (see figure 5), consists of two different overall shock wave configurations, an oMR (figure 4*b*) and an oRR (figure 4*c*), for the same flow conditions. It is described, in figure 9, by the loop S-N-O-P-R-S. The second one, the minor one, has not been recorded experimentally, probably because of the poor experimental resolution along the surface of the mobile cone. It consists of only oMR shock wave configurations (figure 4*b*), but different flow patterns for the same flow conditions. Figure 9 reveals four such minor hysteresis loops, namely B-C-D-W-B, E-F-G-V-E, H-I-J-U-H and K-L-M-T-K.

These two different types of hysteresis loops will be presented in the following: the major one, which is the more important one, i.e. the S-N-O-P-R-S loop, will be treated first. The numerical results will be presented using lines of constant density (i.e. isopycnics).

*The major S-N-O-P-R-S hysteresis loop*

The major S-N-O-P-R-S hysteresis loop is shown in figure 10. The stable numerical flow patterns, on shifting $X$ from 1.3 to 0.7 and back to 1.3, are presented. As mentioned earlier this hysteresis, which is non-viscous dependent, is probably driven by a dual-solution-domain mechanism. The calculated wave configuration for $X = 1.3$ is shown in figure 10($a$). It is an oRR, similar to the one shown schematically in figure 4($c$). The incident converging straight conical and the incident diverging curvilinear conical shock waves intersect each other in a regular manner. The refracted converging conical shock wave reflects from the surface of the mobile cone as a regular reflection, RR. The reflected shock wave of this RR interacts with the refracted diverging curvilinear conical shock wave. When $X$ is decreased to 0.80 (see figure 10$b$) the reflection of the transmitted converging conical shock wave from the surface of the mobile cone changes from a regular reflection, RR, to a Mach reflection, MR. Upon a further decrease in $X$ to 0.70 (see figure 10$c$) a drastic change occurs. The overall wave configuration changes suddenly from an oRR, to an oMR. If the direction of shifting the mobile cone is now reversed and $X$ is increased back towards its initial value of $X = 1.3$ , the flow patterns shown in figures 10($d$) to 10($e$) are found. The length of the Mach stem of the oMR wave configurations decreases gradually. In addition, it is evident from figures 10($c$) to 10($e$) that once an oMR is formed the interaction of the wave reflected from the surface of the mobile cone and the contact surface results in a special structure of 'humps' of the contact surface. (It is important to note here that a very similar wave configuration, including the structure of humps, has been obtained recently by Olejniczak, Wright & Candler (1997) who investigated numerically the interaction on double-wedge geometries in a two-dimensional planar flow.) The number of humps of the contact surface is seen to increase as $X$ is increased. A close inspection of figure 10 indicates that there are three full humps for $X = 0.70$ and 0.80 (figures 10$c$ and 10$d$, respectively) and seven full humps for $X = 1.3$) (figure 10$e$). The two pairs shown in figures 10 ($b, d$) (for $X = 0.8$) and 10($a, e$) (for $X = 1.3$), which show different overall shock wave configurations for identical flow conditions, provide clear evidence of the hysteresis phenomenon. The subsonic flow regions are shaded in figures 10($a$) to 10($e$). The fact that supersonic boundary conditions are present for all the downstream boundaries clearly verifies that the above-mentioned pairs (i.e. $b, d$ and $a, e$) are indeed different flow configurations that result from a hysteresis effect.

As can be seen in figure 10 the oRR $\rightarrow$ oMR transition, i.e. the transition from an overall RR wave configuration (figure 10$b$) to an overall MR wave configuration (figure 10$c$), takes place at $X \approx 0.75$.

A remark regarding the 'wiggles' in the contours plotted (see e.g. figure 10), which originate from the reflected oblique shock in the supersonic portion of the flow field, is needed here. Although these 'wiggles' give an impression that the quality of the numerical results is impaired, one should note that such fluctuations are characteristic for schemes of second order-accuracy in the following situations:

(i) slowly moving (with respect to the mesh) strong shock waves in one-dimensional unsteady flows; and (ii) strong shock waves with small angles between the shock fronts and the mesh lines in two-dimensional steady flows.

The latter situation is encountered in the present calculations. There are quite a few studies which purport to diminish this undesirable numerical effect (see e.g. Arora & Roe 1997; Karni & Ćanić 1997; Jin & Liu 1997; Sokolov *et al.* 1999). In these studies some efficient methods for damping the 'wiggles' in second-order schemes were
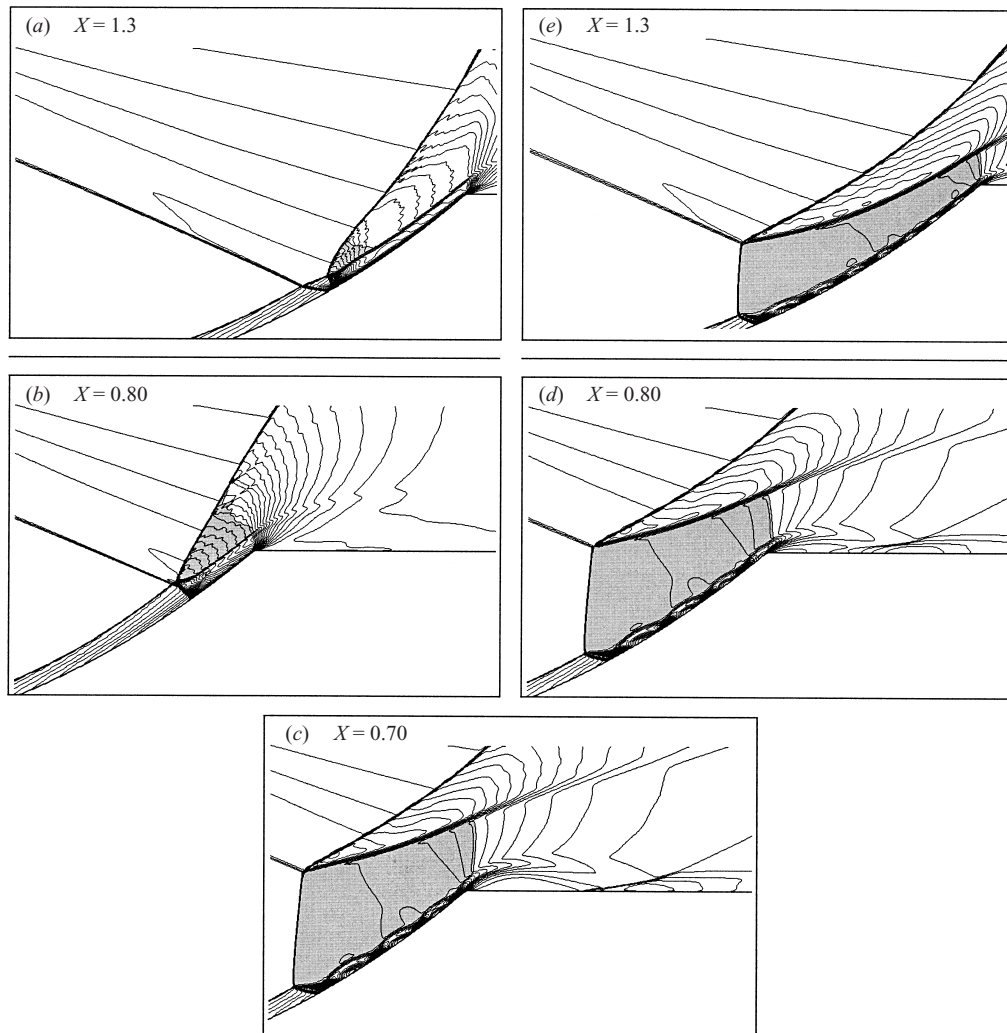
FIGURE 10. Numerical results illustrating the major S-N-O-P-R-S hysteresis loop of figure 9. The subsonic flow regions are shaded.

developed for one-dimensional flows while the problem for the two-dimensional flows is still unsolved. For this reason it is concluded by Arora & Roe (1997) that 'It is quite possible that there is, in general, no completely satisfactory solution to this problem'. In the present study most of the 'wiggles' were eliminated by using a procedure for tracking the Mach stem. Further smoothing could be achieved by using artificial viscosity. However, this would have reduced the accuracy of the scheme to that of a first-order one and would have smeared the contact surfaces. Since it was believed that this is unacceptable it was decided to keep low-dissipation of the scheme along the streamlines. As a result, small density inhomogeneities, which were formed at the reflected wave front, were conserved along the trajectories of the particles while they attenuated quite strongly along other directions and also for other flow parameters such as pressure.

Finally, it is important to note that the propagation of small inhomogeneities along the streamlines behind the reflected shock wave has absolutely no effect on

the phenomenon investigated since all the principal gasdynamic effects occur in the region near the cone surface and in the subsonic region behind the Mach stem.

*Comparison of the simulation and the experimental results*

Two hysteresis loops were detected in the course of the present experimental investigation: the viscous-dependent hysteresis loop (figure 3) and an internal non-viscous-dependent hysteresis loop (figure 5). Since the numerical simulations were performed with an inviscid code, the main attention in the calculations was paid to investigating the non-viscous-dependent hysteresis loop. The numerical hysteresis, shown in figure 10, has features both in common and distinct from the experimental hysteresis that was shown in figure 5. On shifting the mobile cone towards the conical ring (i.e. reducing $X$) the oRR $\rightarrow$ oMR transition takes place: see the change in the wave configurations on moving from frame (*c*) to frame (*d*) in figure 5 (the experimental hysteresis) and from frame (*b*) to frame (*c*) in figure 10 (the numerical hysteresis). However, in the numerical calculations the transition occurred considerably later than in the experiments. This difference can be attributed to the boundary layers inside the conical ring and along the surface of the mobile cone. These boundary layers change the angles between the interacting incident shock waves, and affect the flow near the surface of the mobile cone and downstream of the interaction point (e.g. local separation zones in the boundary layer). The latter conclusion is supported by the fact that while in the numerical calculations the oRR $\rightarrow$ oMR transition could not be detected for conical rings having an angle smaller than $\theta = 10.5°$, in the experiments the oRR $\rightarrow$ oMR transition was recorded with a conical ring having an angle $\theta = 8.5°$. The reversed oMR $\rightarrow$ oRR transition when the mobile cone was shifted away from the conical ring occurred in the simulation at a larger value of $X$ than in the experiments. In summary, probably due to a viscous effect, the numerical dual-solution-induced hysteresis loop was found to be larger than the experimental one.

As can be seen in figure 9, the major S-N-O-P-R-S hysteresis loop consists of two transitions: the oRR $\rightarrow$ oMR transition between points R and S, which is associated with the sudden appearance of a finite-length Mach stem, and the opposite oMR $\rightarrow$ oRR transition at point P, which is seen to occur where the Mach stem vanishes, i.e. $H_m \rightarrow 0$.

The inviscid numerical simulation failed, as expected, to reproduce the viscous-dependent hysteresis loop shown in figure 5. However, the detailed numerical investigation using the inviscid model revealed fine hysteresis loops, which were caused by the interaction of the above-mentioned humps associated with the oMR wave configuration with the rear edge of the mobile cone. These hysteresis loops will be discussed subsequently.

The oMR wave configuration (see e.g. figure 10*c*) consists of two MR wave configurations. The upper one is an inverse-Mach reflection, $I_nMR$, and the lower one is a direct-Mach reflection, $D_iMR$ (for details regarding the inverse-Mach reflection see Ben-Dor 1991). The reflected shock wave of the lower MR is reflected from the surface of the mobile cone as a regular reflection, RR. The reflected shock wave of this RR interacted with the contact surface of the lower MR. Since the flow field was subsonic above the contact surface and supersonic below it the reflection from the contact surface, of a wave approaching from the supersonic side, was almost total, i.e. shock and compression waves reflected as expansion waves and expansion waves reflected as compression waves. When these waves reflected from the solid surface of the mobile cone they did not change their nature, i.e. expansion waves reflected as
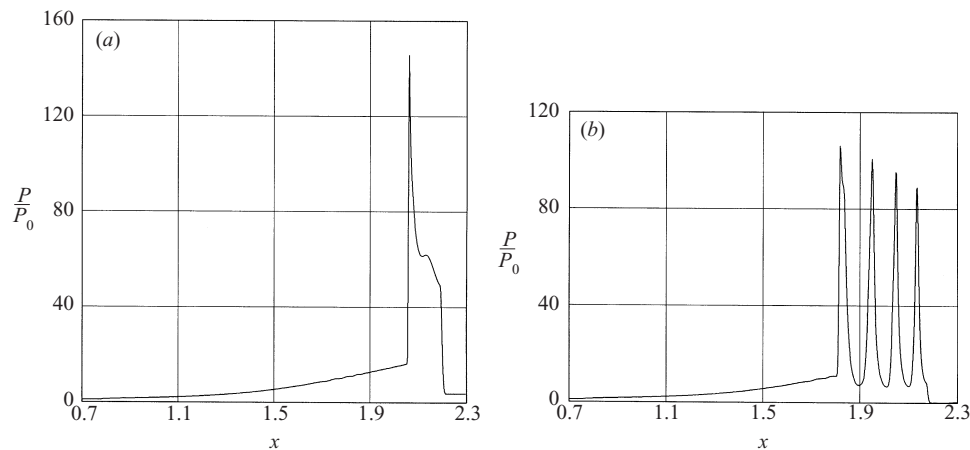
FIGURE 11. Pressure profiles along the surface of the curvilinear mobile cone: (*a*) for an oRR at $X = 0.76$ (similar to that shown in figure 10*b*), (*b*) for an oMR at $X = 0.76$ (similar to that shown in figure 10*c*). The pressure peaks correspond to the edges of the full humps of the contact surface.

expansion waves and compression waves reflected as compression waves. As a result an almost periodic structure of humps of the contact surface was formed. Three full stable humps are seen in figure 10(*c*). Five, seven and nine humps were obtained in the calculations (not shown here) for $X = 1.0$, $X = 1.25$ and $X = 1.4$, respectively. (It is important to note here again that a very similar wave configuration including the special structure of humps was obtained by Olejniczak *et al.* 1997 who investigated numerically the shock interaction on double-wedge geometries in a two-dimensional planar flow, compare figure 10(*c*) with figure 13(*b*) in Olejniczak *et al.* 1997.)

As will be shown subsequently, the $X$-coordinate of the mobile cone when a given hump detached from the rear edge of the mobile cone was found to be different from the $X$-coordinate of the mobile cone when the same hump reattached. This in turn led to the identification of additional hysteresis loops in which the wave configuration was always an oMR but the flow patterns along the surface of the mobile cone were different. These minor hysteresis loops are shown in figure 9 as B-C-D-W-B, E-F-G-V-E, H-I-J-U-H and K-L-M-T-K.

The pressure distributions along the surface of the mobile cone for the case with an oRR wave configuration (at $X = 0.76$) and for the case with an oMR wave configuration (at $X = 0.76$) are shown in figures 11(*a*) and 11(*b*), respectively. A dramatic change in the pressure profile along the surface of the mobile cone is evident. The single pressure peak, which is seen in figure 11(*a*), is associated with the Mach stem of the MR wave configuration (see e.g. figure 10*b*). The four pressure peaks, which are seen in figure 11(*b*), are associated with the four edges of the three humps of the contact surface (see e.g. figure 10*c*). It is evident from figure 11(*b*) that the first pressure peak exceeds 100 times the ambient pressure. It is also seen that the pressures are about 10 times larger at the edges of the humps of the contact surface than at their centres. The pressure peaks are seen to decrease, by about 5–7%, from hump to hump. It is interesting to note that pressure profiles similar to those shown in figure 11(*b*) were obtained in the above-mentioned study of Olejniczak *et al.* (1997) in which, as indicated earlier, similar wave configurations were obtained. In a typical calculation presented (see figure 14 in Olejniczak *et al.* 1997) the pressures were about 250–400 times larger at the edges of the humps of the contact surface than at their

centres. It is important to note that the narrowly localized alternating pressure peaks could impose considerable dynamic and thermal loads on the surface of the mobile cone.

*The minor B-C-D-W-B, E-F-G-V-E, H-I-J-U-H and K-L-M-T-K hysteresis loops*

As mentioned earlier, the location of the mobile cone when a given hump detached from the rear edge of the mobile cone was found to be different from the location of the mobile cone when the same hump reattached. The attachment/detachment mechanism led to the identification of additional minor hysteresis loops in which the wave configuration was always an overall Mach reflection, oMR, but the flow patterns along the surface of the mobile cone were different. These minor hysteresis loops, which are shown in figure 9 as B-C-D-W-B, E-F-G-V-E, H-I-J-U-H and K-L-M-T-K, are presented in the following.

*The B-C-D-W-B hysteresis loop*: The B-C-D-W-B hysteresis loop is shown in figure 12, where the stable numerical flow patterns, for a variation of $X$ from 0.02 to 0.26 and back to 0.02, are presented. At $X = 0.02$ (figure 12a) an oMR wave configuration is obtained. It should be noted that, unlike the previously discussed oMR wave configurations where the reflected shock wave of the lower MR interacted with the mobile cone upstream of its rear edge, here it interacts with the surface of the mobile cone downstream of its rear edge. An inspection of the orientation of the upper contact surface indicates that the upper Mach reflection is an inverse-Mach reflection, $I_nMR$. When $X$ is increased (see figures 12b and 12c) the Mach stem connecting the two triple points moves upstream and its length increases. Note that a situation in which the reflected shock wave of the lower MR touches the rear edge of the mobile cone is reached in the vicinity of $X = 0.20$ (see figure 12c). An increase of $X$ beyond this value results in a sudden jump of the Mach stem upstream which is associated with a sudden increase in the length of the Mach stem, as shown in figure 12(d) for $X = 0.26$. The sudden transition results in a wave configuration in which the reflected shock wave of the lower MR reflects as an RR from the surface of the mobile cone. Note also that the contact surface of the upper MR, i.e. the $I_nMR$, has straightened out. When $X$ is decreased back to $X = 0.02$ the stable solutions shown in figures 12(e) to 12(g) are obtained. The two pairs $(c, e)$ (for $X = 0.20$) and $(b, f)$ (for $X = 0.12$) which show different overall wave configurations for identical flow conditions are clear evidence of the hysteresis. The hysteresis is typified by a sudden increase in the length of the Mach stem at $X \approx 0.23$ and a reversed sudden decrease in the length of the Mach stem at $X \approx 0.05$. The calculations revealed that the mechanism, which triggers the sudden transition from an oMR with a short Mach stem (figure 12c) to an oMR with a much larger Mach stem (figure 12d), is the interaction of the reflected shock wave of the lower MR with the rear edge of the mobile cone (see figure 12c). Note that once the transition takes place (see figure 12d) the reflected shock wave of the lower MR reflects from the surface of the mobile cone as an RR. The reflected shock wave of this RR interacts with the contact surface of the lower MR. The result of this interaction is an expansion wave, which hits the surface of the mobile cone and reflects back towards the contact surface as an expansion wave. The reflected expansion wave interacts with the contact surface and causes it to turn back towards the mobile cone. Had $X$ been further increased, as will be shown subsequently, this turn of the contact surface would have been developed to become the first full hump of the contact surface. Figures 12(f) and 12(g) indicate that the reverse transition is driven by the interaction of the above-mentioned expansion wave with the rear edge of the mobile cone.
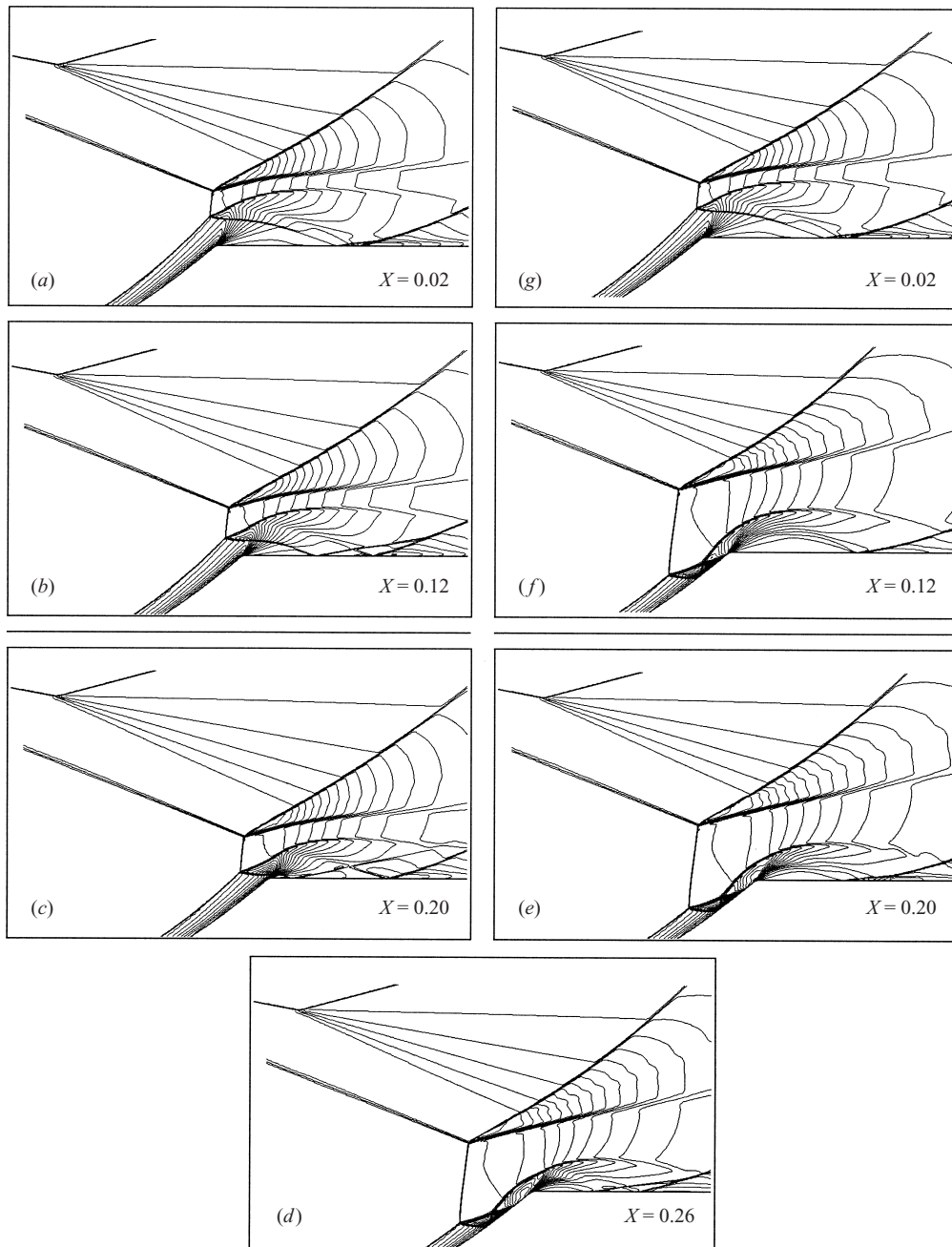
FIGURE 12. Numerical results illustrating the minor B-C-D-W-B hysteresis loop of figure 9.

It should be noted here that at least one additional stable wave configuration exists in the range of $X$ shown in figure 12. This wave configuration, which is shown in figure 13 for $X = 0.10$, consists of a regular interaction between the incident converging straight conical and the incident diverging curvilinear conical shock waves. The numerical flow pattern shown in figure 13 was obtained artificially by introducing perturbations into the stationary flow pattern shown in figure 12(*a*) or 12(*g*) (i.e. by
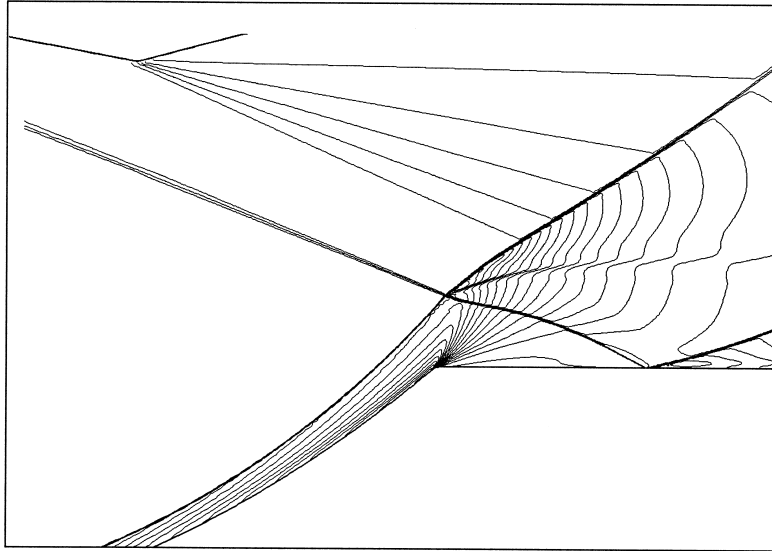
FIGURE 13. An additional stable wave configuration, which exists in the range of $X$, which is covered in figure 12. The wave configuration resembles a regular interaction between the incident converging straight conical and the incident diverging curvilinear conical shock waves. This numerical flow pattern was obtained artificially by introducing perturbations into the stationary flow pattern shown in figure 12($g$).

artificially increasing the gas velocity behind the Mach stem) and simultaneously moving the cone to $X = 0.10$. The perturbation-driven stable oRR, which is shown in figure 13, could be obtained in the range $0.04 \leqslant X \leqslant 0.10$.

*The minor E-F-G-V-E hysteresis loop*: The minor E-F-G-V-E hysteresis loop is shown in figure 14, where the stable numerical flow patterns, for a variation of $X$ from 0.26 to 0.38 and back to 0.26, are presented. Note that all the upper MRs are inverted. In addition, the contact surfaces of these $I_n$MRs are straight (recall that the flow is axisymmetric). At $X = 0.26$ (figure 14$a$) an oMR is obtained. When $X$ is increased (see figure 14$b$) the Mach stem connecting the two triple points moves upstream and its length increases. The flow patterns in figures 14($a$) and 14($b$) for $X = 0.26$ and 0.34, respectively, are similar to that shown in figure 12($f$). A further increase to $X = 0.38$ results in the flow pattern shown in figure 14($c$), in which the above-mentioned expansion wave developed a full hump of the contact surface of the lower MR. When $X$ is decreased back to $X = 0.26$ the stable flow patterns shown in figures 14($d$) and 14($e$) are obtained. The pair ($b$, $d$) (for $X = 0.34$) that shows different flow patterns for identical flow conditions is clear evidence of the hysteresis, typified by a sudden increase in the length of the Mach stem at a value of $X$ in the range $0.34 \leqslant X \leqslant 0.38$, and a sudden decrease in the length of the Mach stem at a value of $X$ in the range $0.26 \leqslant X \leqslant 0.30$. It is evident from figure 14 that the hysteresis is driven by a mechanism associated with the attachment/detachment of the first hump to/from the surface of the mobile cone. For this reason the hysteresis loop, shown in figure 14, can be termed as 0 hump $\leftrightarrow$ 1 hump hysteresis.

Based on detailed calculations in this range it is quite clear that the mechanism that triggers the sudden transition from an oMR with a short Mach stem (figure 14$b$) to an oMR with a larger Mach stem (figure 14$c$) is the interaction of the second reflected compression wave with the rear edge of the mobile cone. Note that once the transition takes place a full stable hump of the contact surface is established
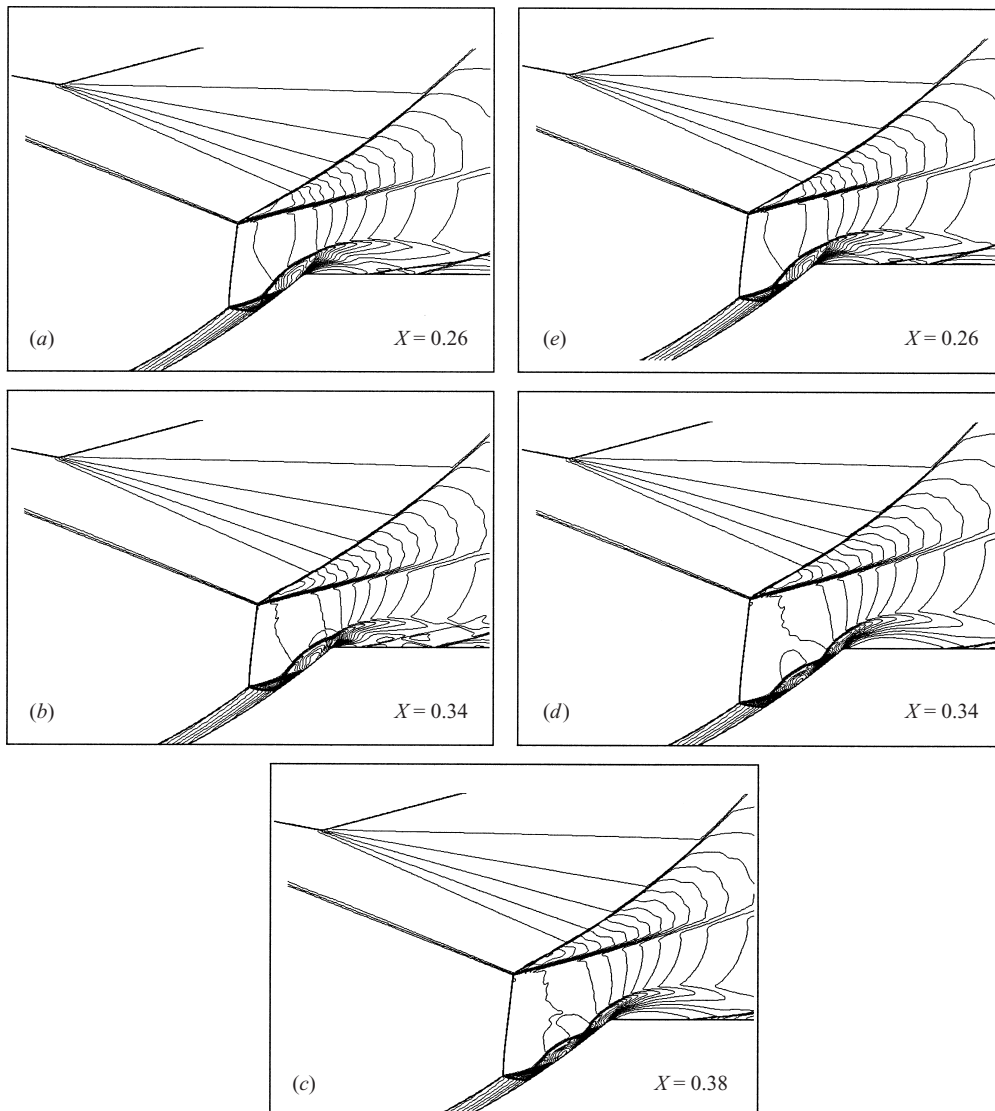
FIGURE 14. Numerical results illustrating the minor E-F-G-V-E hysteresis loop of figure 9. As can be seen the hysteresis is associated with the attachment/detachment of the first hump of the contact surface to/from the surface of the mobile cone.

over the surface of the mobile cone. The 0 hump → 1 hump transition was found to occur at $X \approx 0.37$. The calculations also revealed that the reversed 1 hump → 0 hump transition is driven by the interaction of the downstream edge of the first hump of the contact surface with the rear edge of the mobile cone. The 1 hump → 0 hump transition was found to occur at $X \approx 0.27$.

*The minor H-I-J-U-H hysteresis loop*: The minor H-I-J-U-H hysteresis loop is shown in figure 15. The stable numerical flow patterns, for a variation of $X$ from 0.46 to 0.56 and back to 0.46, are presented. At $X = 0.46$ (figure 15a) an oMR with one full stable hump of the contact surface is obtained. When $X$ is increased the Mach stem connecting the two triple points moves upstream and its length increases, until $X$ is
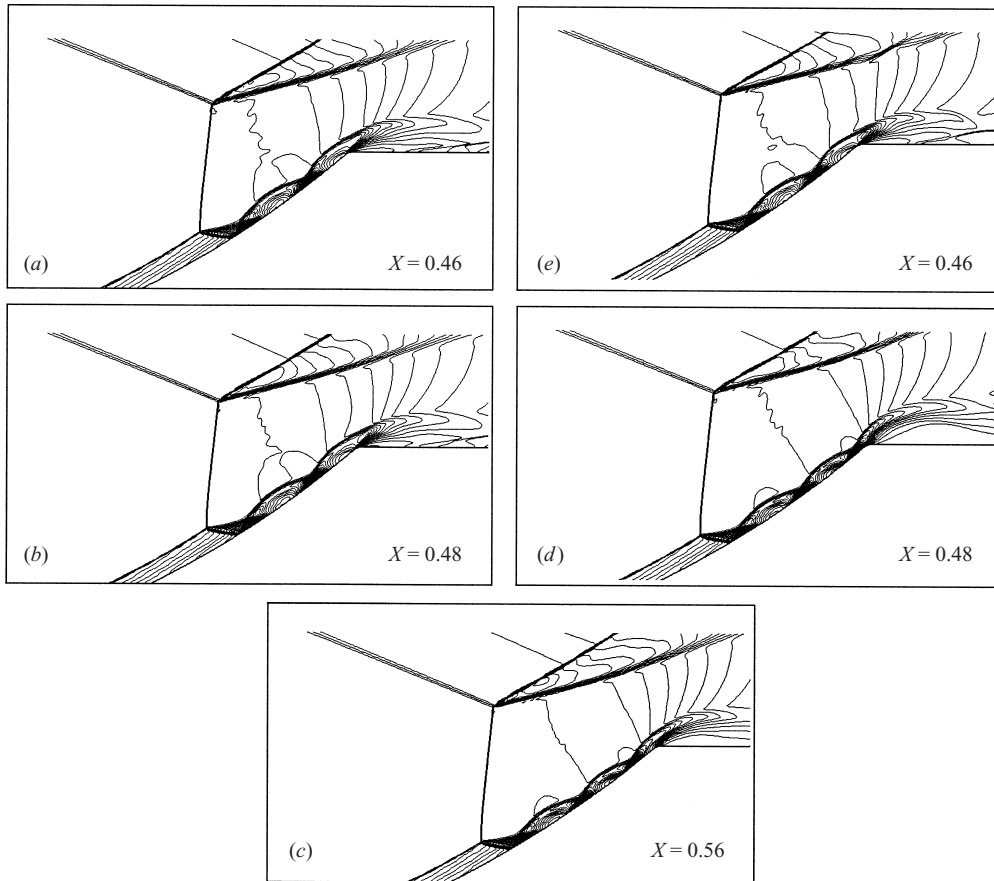
FIGURE 15. Numerical results illustrating the minor H-I-J-U-H hysteresis loop of figure 9. As can be seen the hysteresis is associated with the attachment/detachment of the second hump of the contact surface to/from the surface of the mobile cone.

increased to $X = 0.56$ at which the flow pattern shown in figure 15(c), in which the above-mentioned expansion wave developed two full humps of the contact surface of the lower MR. When $X$ is decreased back to $X = 0.46$ the stable flow patterns shown in figures 15(d) and 15(e) are obtained. The pair (b, d) (for $X = 0.48$) which show different overall flow patterns for identical flow conditions is clear evidence of the hysteresis, typified by a sudden increase in the length of the Mach stem at $X \approx 0.55$ and a sudden decrease in the length of the Mach stem at $X \approx 0.47$. It is evident from figure 15 that the hysteresis is driven by a mechanism associated with the attachment/detachment of the second hump to/from the surface of the mobile cone. For this reason the hysteresis loop shown in figure 15 can be termed a 1 hump ↔ 2 humps hysteresis. Detailed calculations indicated that the mechanism that triggers the sudden transition from an oMR with a short Mach stem to an oMR with a larger Mach stem is the interaction of the reflected third compression wave with the rear edge of the mobile cone. Note that once the transition takes place two full stable humps of the contact surface are established over the surface of the mobile cone. The 1 hump → 2 humps transition was found to occur at $X \approx 0.55$. The calculations also revealed that the reversed 2 humps → 1 hump transition is driven by the interaction of the downstream edge of the second hump of the contact
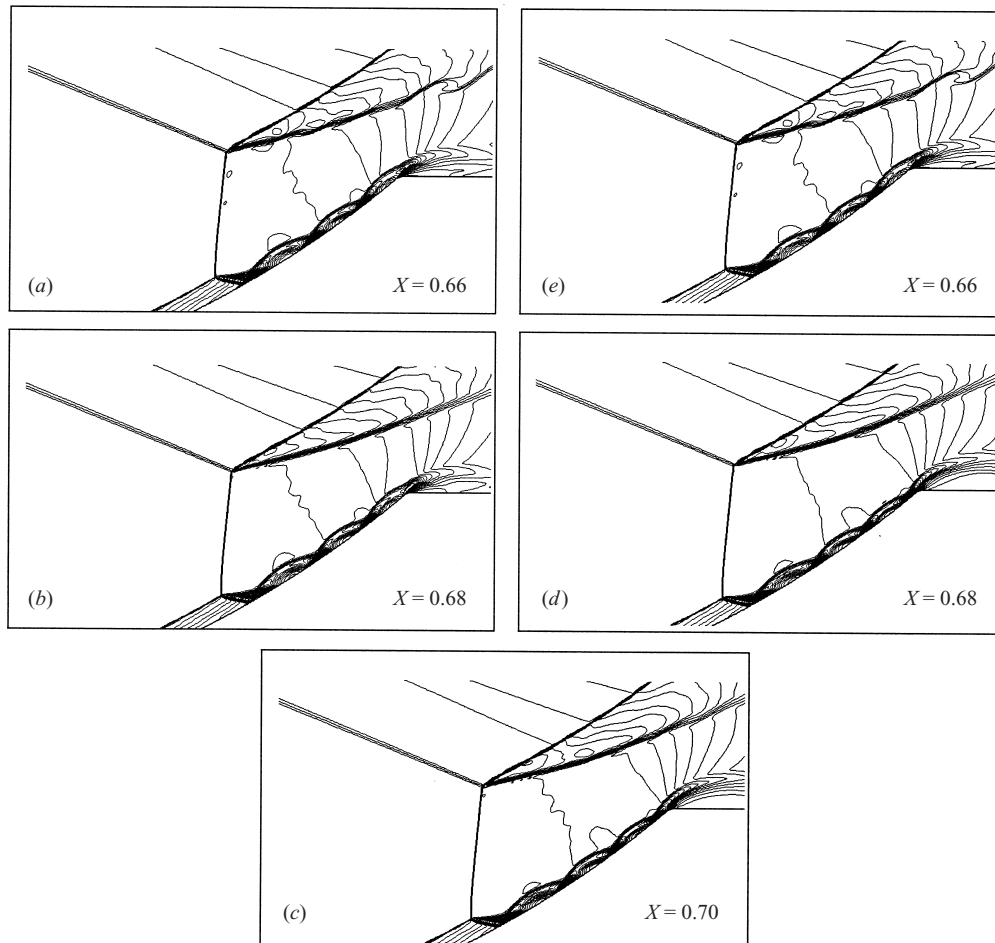
FIGURE 16. Numerical results illustrating the minor K-L-M-T-K hysteresis loop of figure 9. As can be seen the hysteresis is associated with the attachment/detachment of the third hump of the contact surface to/from the surface of the mobile cone.

surface with the rear edge of the mobile cone. Based on figure 15($d$) and 15($e$) the 2 humps $\rightarrow$ 1 hump transition occurs at $X \approx 0.47$.

*The minor K-L-M-T-K hysteresis loop*: The minor K-L-M-T-K hysteresis loop is shown in figure 16, where stable numerical flow patterns, for a variation of $X$ from 0.66 to 0.70 and back to 0.66, are presented. At $X = 0.66$ (figure 16$a$) an oMR with two full stable humps of the contact surface is obtained. When $X$ is increased to $X = 0.68$ (see figure 16$b$) the Mach stem connecting the two triple points moves upstream and its length increases. A further increase to $X = 0.70$ results in the flow pattern shown in figure 16($c$), in which the above mentioned expansion wave developed three full humps of the contact surface of the lower MR. When $X$ is decreased back to $X = 0.66$ the stable flow patterns shown in figures 16($d$) and 16($e$) are obtained. Similarly to the two previous cases the pair $(b, d)$ (for $X = 0.68$), which show different overall flow patterns for identical flow conditions, is clear evidence of the hysteresis, typified by a sudden increase in the length of the Mach stem at $X \approx 0.69$ and a sudden decrease in the length of the Mach stem at $X \approx 0.67$. It is evident from figure 16 that the

hysteresis is driven by a mechanism associated with the attachment/detachment of the third hump to/from the surface of the mobile cone. For this reason the hysteresis loop shown in figure 16 can be termed a 2 humps ↔ 3 humps hysteresis.

Again similarly to the two previous cases, it is quite clear that the mechanism that triggers the sudden transition from an oMR with a short Mach stem (figure 16b) to an oMR with a larger Mach stem (figure 16c) is the interaction of the fourth compression wave with the rear edge of the mobile cone. Note that once the transition takes place three full stable humps of the contact surface are established over the surface of the mobile cone (see figure 16c). Consequently, the 2 humps → 3 humps transition occurs at $X \approx 0.69$. The reversed 3 humps → 2 humps is driven by the interaction of the downstream edge of the third hump of the contact surface with the rear edge of the mobile cone. Based on figures 16(d) and 16(e) the 3 humps → 2 humps transition occurs at $X \approx 0.67$.

## 4. Discussion and conclusion

The interaction of two conical shock waves, one converging and straight and the other diverging and curvilinear, in an axisymmetric flow was investigated both experimentally and numerically.

A double-loop hysteresis was discovered in the course of the experimental investigation. It consisted of a major loop, associated with the interaction between the boundary layer and the wave configuration, and a minor loop, associated with the dual-solution phenomenon, which is known to be non-viscous-dependent. The minor hysteresis loop was found to be an internal hysteresis loop of the major one. The experimental results revealed a hysteresis in a flow field that was by definition free of three-dimensional effects.

The numerical Euler calculations failed, as expected, to detect the viscous-dependent major hysteresis loop but did succeed in obtaining the non-viscous-dependent minor hysteresis loop. In addition, multiple minor hysteresis loops, associated with the interaction between the shock wave configuration and the edge of the curvilinear mobile cone were also observed. The non-viscous internal hysteresis loop involved different overall shock wave reflection configurations, and the other minor hysteresis loops involved MR wave configurations with different flow patterns.

A very interesting phenomenon has been observed in the flow field near the mobile cone, in the cases in which the overall flow pattern consisted of a Mach reflection wave configuration. The reflected shock wave, which emerged from the lower triple point towards the surface of the mobile cone, reflected from it as a regular reflection. The reflected shock wave of this regular reflection interacted with the contact surface emerging from the lower triple point. Since the flow field was subsonic above the contact surface and supersonic below it the reflection from the contact surface, of a wave from the supersonic side, was almost total, i.e. compression waves reflected as expansion waves and expansion waves reflected as compression waves. When these waves reflected from the solid surface of the mobile cone they did not change, i.e. expansion waves reflected as expansion waves and compression waves reflected as compression waves. As a result an almost periodic structure of humps of the contact surface was formed. In fact the structure is similar to that occurring in a supersonic weakly over-expanded jet (without Mach stems). The only difference was that, in the present case, the surface of the mobile cone played the role of a 'symmetric axis', and therefore only 'half' of the jet was observed. A very similar wave configuration,

including the structure of humps, was obtained by Olejniczak *et al.* (1997) who studied shock interactions with double-wedge geometries in two-dimensional flows.

As a result of the interaction of the contact surface with the alternating compression and expansion waves, which bounced back and forth between the contact surface and the surface of the mobile cone, the contact surface developed a structure that consisted of stable humps: flow patterns consisting of one to nine humps were obtained. It was shown that the transition and the reversed transition between adjacent structures, i.e. the appearance/disappearance or attachment/detachment of full stable humps along the surface of the mobile cone, occurred at different locations on the mobile cone. This in turn led to a situation in which the phenomenon was associated with additional minor hysteresis loops, in which the shock wave configuration was always an overall Mach reflection but the flow patterns were different.

As a result of this flow pattern an interesting focusing process takes place. Pressure and density peaks developed along the surface of the mobile cone at the successive edges of the humps of the contact surface (see for example the pressure profile shown in figure 11*b* for the case of three humps).

Both the experimental and the numerical results clearly indicated that the investigated shock wave interaction phenomenon is associated with multi hysteresis loops. Furthermore, the experimental results provided clear evidence of a hysteresis in the shock wave interaction process in an axisymmetric flow field that absolutely is free of three-dimensional effects.

It is important to note that the motivation for conducting the numerical investigation that is reported in this study was the experimental results. Owing to the use of an inviscid code the code failed, as expected, to obtain the experimentally observed viscous-dependent hysteresis loop. However, the code did succeed in obtaining the experimental dual-solution-domain driven hysteresis loop. The differences, which were found to exist between the experimental and the numerical dual-solution-domain driven hysteresis loops, were attributed to boundary layer effects along the surface of the mobile cone. Owing to the poor resolution along the surface of the mobile cone, the multi minor hysteresis loops, which were found numerically, were not observed experimentally. Consequently, the present study provides a clear example of the advantage of numerical simulations over real experiments when very fine details of the flow field are needed.

## REFERENCES

ARORA, M. & ROE, L. R. 1997 On post-shock oscillations due to shock capturing schemes in unsteady flows. *J. Comput. Phys.* **130**, 25–40.

BEN-DOR, G. 1991 *Shock Wave Reflection Phenomena.* Springer.

BEN-DOR, G., ELPERIN, T., LI, H. & VASILIEV, E. 1999 The influence of downstream-pressure on the shock wave reflection phenomenon in steady flows. *J. Fluid Mech.* **386**, 213–232.

BURSTCHELL, Y., ZEITOUN, D. E., CHPOUN, A. & BEN-DOR, G. 2001 Conical shock interactions in a steady flow. Numerical study, presented at the *23rd Intl Symp. on Shock Waves, Fort Worth, Texas.*

CHPOUN, A., CHAUVEUX, F., ZOMBAS, L. & BEN-DOR, G. 1999 Interaction d'onde de choc coniques

de familles opposées en écoulement hypersonique stationnaire, Mécanique des Fluides/Fluid Mechanics. *C. R. Acad. Sci. Paris* **327**, IIb, 85.

CHPOUN, A. & LENGRAND, J. C. 1997 Conférmation expérimentale d'un phénomène d'hystérésis lors de l'interaction de deux chocs obliques de familles différentes. *C. R. Acad. Sci. Paris* **304**, 1.

CHPOUN, A., PASSEREL, D., LI, H. & BEN-DOR, G. 1995 Reconsideration of oblique shock wave reflection in steady flows. Part 1. Experimental investigation. *J. Fluid Mech.* **301**, 19–35.

FOMIN, V. M., HORNUNG, H. G., IVANOV, M. S., KHARITONOV, A. M. & KLEMENOV, G. P. 1996 The study of transition between regular and Mach reflection of shock waves in different wind tunnels. *Book of Abstracts, 12th Intl Mach Reflection Symp., Johannesburg, South Africa.*

HORNUNG, H. G., OERTEL, H. & SANDEMAN, R. J. 1979 Transition to Mach reflection of shock waves in steady and pseudo-steady flow with and without relaxation. *J. Fluid Mech.* **90**, 541–560.

IVANOV, M. S., GIMELSHEIN, S. F., KUDRYAVTSEV, A. N. & MARKELOV. G. N. 1998a Transition from regular to Mach reflection in two- and three-dimensional flows. *Proc. 21st Intl Symp. Shock Waves (Great Keppel, Australia, 20–25 July 1997)*, vol. 2, p. 8, Panther Publ.

IVANOV, M. S., KLEMENKOV, G. P., KUDRYAVTSEV, A. N., NIKIFOROV, S. B., PAVLOV, A. A., FOMIN, V. M., KHARITONOV, A. M., KHOTYANOVSKY, D. V. & HORNUNG, H. G. 1998b Experimental and numerical study of the transition between regular and Mach reflections of shock waves in steady flows. *Proc, 21st Intl Symp. Shock Waves (Great Keppel, Australia, 20–25 July 1997)*, vol. 2, p. 819, Panther Publ.

JIN, S. & LIU, J.-G. 1997 The effect of numerical viscosities I: Slowly moving shocks. *J. Comput. Phys.* **126**, 373–389.

KARNI, S. & ĆANIĆ, S. 1997 Computations of slowly moving shocks. *J. Comput. Phys.* **136**, 132–139.

KRASIL'NIKOV, A. V. 1991 Experimental investigation of the interaction between convergent axisymmetric shock waves and sharp and blunt cones in supersonic flow. *Fluid Dyn.* **26**, 784.

LI, H., CHPOUN, A. & BEN-DOR, G. 1999 Analytical and experimental investigations of the reflection of asymmetric shock waves in steady flows. *J. Fluid Mech.* **390**, 25–43.

MACH, E. 1878 Uber den Verlauf von Funkenwellen in der Ebene und im Raume. *Sitzungsbr. Akad. Wiss. Wien* **78**, 819.

NEUMANN, J. VON 1945 Refraction, intersection and reflection of shock waves. *NAVORD Rep.* 203–45. Navy Dept., Bureau of Ordinance, Washington, DC, USA.

OLEJNICZAK, J., WRIGHT, M. J. & CANDLER, G. V. 1997 Numerical study of inviscid shock interactions of double-wedge geometries. *J. Fluid Mech.* **352**, 1–25.

RYLOV, A. I. 1990 On the impossibility of regular reflection of a steady-state shock wave from the axis of symmetry. *J. Appl. Math. Mech.* **54**, 200–203.

SKEWS, B. W. 1997 Aspect ratio effects in wind tunnel studies of shock wave reflection transition. *Shock Waves* **7**, 373.

SKEWS, B. W. 1998 Oblique shadowgraph study of shock wave reflection between two wedges in supersonic flow. *Book of Abstracts, 13th Intl Mach Reflection Symp., Beer Sheva, Israel.*

SKEWS, B. W., VUKOVIC, S. & DRAXL, M. 1996 3D effects in steady flow shock wave reflection transition. *Proc. 12th Intl Mach Reflection Symp., University of Witwatersrand, South Africa*, pp. 152–162.

SOKOLOV, V., TIMOFEEEV, E. V., SAKAI, J. & TAKAYAMA, K. 1999 On shock-capturing schemes using artificial wind. *Shock Waves* **9**, 423–427.

VASILIEV, E. I. 1996 A W modification of Godunov's method and its application to two-dimensional non-stationary flows of dusty gas. *Comput. Math. Math. Phys.* **36**, 101–112.

VASILIEV, E. I. & KRAIKO, A. N. 1999 Numerical simulation of weak shock diffraction over a wedge under the von Neumann paradox conditions. *Comput. Math. Math. Phys.* **39**, 1345–1355.